Using a Dense Seismic Array to Determine Structure and Site Effects of the Two Towers Earthflow in Northern California

Amanda M. Thomas*[1], Zack Spica[2], Miles Bodmer[1], William H. Schulz[3], and Joshua J. Roering[1]

Abstract

We deployed a network of 68 three-component geophones on the slow-moving Two Towers earthflow in northern California. We compute horizontal-to-vertical spectral ratios (HVSRs) from the ambient seismic field. The HVSRs have two prominent peaks, one near 1.23 Hz and another between 4 and 8 Hz at most stations. The 1.23 Hz resonance is a property of the background noise field and may be due to a velocity contrast at a few hundred meters depth. We interpret the higher frequency peaks as being related to slide deposits and invert the spectral ratios for shallow velocity structure using *in situ* thickness measurements as *a priori* constraints on the inversion. The thickness of the shallowest, low-velocity layer is systematically larger than landslide thicknesses inferred from inclinometer data acquired since 2013. Given constraints from field observations and boreholes, the inversion may reflect the thickness of deposits of an older slide that is larger in spatial extent and depth than the currently active slide. Because the HVSR peaks measured at Two Towers are caused by shallow slide deposits and represent frequencies that will experience amplification during earthquakes, the depth of the actively sliding mass may be less relevant for assessing potential slide volume and associated hazard than the thicknesses determined by our inversions. More generally, our results underscore the utility of combining both geotechnical measurements and subsurface imaging for landslide characterization and hazard assessment.

Cite this article as Thomas, A. M., Z. Spica, M. Bodmer, W. H. Schulz, and J. J. Roering (2020). Using a Dense Seismic Array to Determine Structure and Site Effects of the Two Towers Earthflow in Northern California, *Seismol. Res. Lett.* **XX**, 1–8, doi: 10.1785/0220190206.

Supplemental Material

Introduction

Earthquake-induced landslides often cause much of the deaths, damage, and economic losses associated with large earthquakes (e.g., Bird and Bommer, 2004; Yin *et al.*, 2009). In addition to the immediate impacts of coseismically triggered landslides, hazard can remain elevated for years after the earthquake trigger (Hovius *et al.*, 2011). The passage of seismic waves has been shown to weaken hillslopes, which can lead to delayed landslide triggering initiated by subsequent rainfall events (Lin *et al.*, 2008). In addition, material initially transported by landslides becomes more susceptible to erosion, which can result in debris flows, and landslide-dammed rivers can inundate lakes and river valleys, resulting in increased flooding hazard (Owen *et al.*, 2008; Huang and Fan, 2013).

Because of these potential hazards, many geophysical studies aim to characterize landslide properties such as spatial extents, deformation rates, slip surface locations, and so forth. For example, remote sensing is a commonly employed tool for landslide identification and deformation rate estimation (e.g., Delbridge *et al.*, 2016). However, estimates of some physical properties important for hazard, such as the volume, 3D geometry, and location of slip surfaces, require subsurface investigation. Despite its uncertain theoretical basis (Bonnefoy-Claudet *et al.*, 2008; Piña-Flores *et al.*, 2016), Nakamura's method (Nakamura, 1989) has long been used to estimate site resonance frequencies or the frequencies at which ground motions will be amplified. It involves analyzing the ratio of vertical- and horizontal-component spectra of recordings of seismic noise, or the ambient seismic field. The justification for this method is that larger amplitude shear waves are responsible for a majority of the ground motion at a site, and most of their energy is recorded on horizontal channels; thus, peaks in the spectral ratio are thought to represent frequencies that experience local amplification. Recent theoretical advances have also elucidated the relationship between spectral ratios and local velocity structure (Sánchez-Sesma *et al.*, 2011). Because landslides often comprise a soft layer overlaying a more rigid substrate, the base of landslides should represent

---

1. Department of Earth Sciences, University of Oregon, Eugene, Oregon, U.S.A.; 2. Earthquake Research Institute, The University of Tokyo, Tokyo, Japan; 3. U.S. Geological Survey, Denver, Colorado, U.S.A.

*Corresponding author: amthomas@uoregon.edu

a significant impedance contrast, which can be identified in 1D velocity–depth profiles as changes in S-wave velocity. As such, seismic noise–based methods are effective tools for detecting landslide slip surfaces and characterizing landslide structure (Jongmans and Garambois, 2007; Méric *et al.*, 2007; Pazzi *et al.*, 2017, 2019).

Dense observation networks provide the opportunity to estimate structure and site effects in high resolution at the scale of an individual landslide. Here, we use an array of 68 three-component geophones (nodes) deployed on a slow-moving earthflow in northern California to estimate the depth to a landslide slip surface by computing horizontal-to-vertical spectral ratios (HVSRs) from the ambient seismic field at each site and analyzing their peaks, which are thought to represent site resonances. We then explore the physical origins of each HVSR peak by analyzing the ambient seismic field and inverting the full HVSR spectra for shallow structure. Finally, we use our inversions to identify the locations of inferred slip surfaces and compare them with the known locations from independent estimates of landslide thickness determined from slope inclinometer profiling and discuss implications for landslide characterization and hazard estimates.

Methods

Geologic setting and seismic deployment

The focus of the current study is the Two Towers earthflow located within the Eel River catchment of the northern California Coast Ranges (Fig. 1). Earthflows are composed of mostly fine-grained material and experience movement over time periods ranging from days to millennia (Keefer and Johnson, 1983; Hungr *et al.*, 2014). Morphologically, the upslope portion of earthflows consists of an amphitheater-shaped crown, which marks the boundary between undisturbed earth and material associated with the earthflow; a main scarp downslope from which material that composes the earthflow originated; and the head, which contains detached material that is now part of the active portion of the slide. The body of earthflows is typically bound by well-defined lateral shear margins along most of the slide and a rounded toe region that is not typically laterally confined (Keefer and Johnson, 1983; Hungr *et al.*, 2014).

The Two Towers earthflow is 250 m long, averages 40 m wide, and is composed primarily of Franciscan mélange matrix (mixtures of clay, silt, and sand) surrounding competent blocks of sandstone, chert, shale, and minor metamorphosed lithologies (Handwerger *et al.*, 2015; Schulz *et al.*, 2018). The slide lateral boundaries are well developed, nearly vertical shear zones containing heavily striated centimeters-thick gouge (Schulz *et al.*, 2018). Over a 2.5 yr period beginning in November 2014, Schulz *et al.* (2018) made hourly measurements of slide displacement using biaxial tilt sensors installed within polyvinyl chloride-cased (PVC) boreholes. The slide averaged 0.54 mm/week during their study; however, slide movement was episodic in nature with three well-defined slip episodes characterized by slip rates of 0.58, 1.46, and 2.42 mm/week for many weeks (Fig. 1, Schulz *et al.*, 2018). In addition, Schulz *et al.* (2018) used slope inclinometer profiling to estimate thickness at three locations along the slide. They measured basal depths of 6.34, 7.9, and 3.58 m for the head (station 22), middle (station 15), and toe locations (station 3), respectively (blue triangles in Fig. 1). Groundwater was generally within 1–2 m of the ground surface (annual range is within 0–5 m of the ground surface; Schulz *et al.*, 2018).

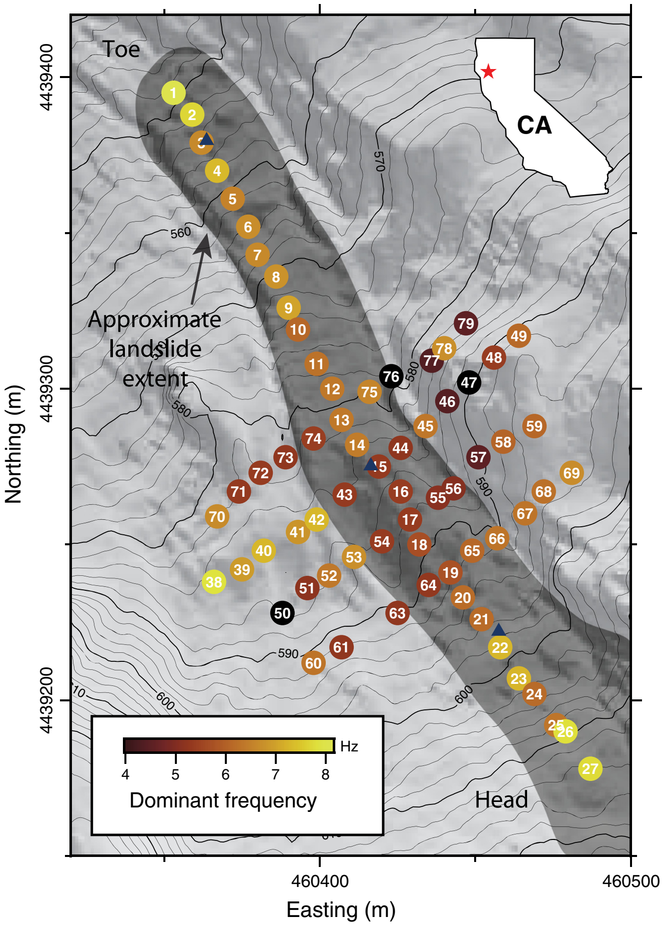

Figure 1. 2016 Two Towers landslide nodal seismometer deployment geometry (UTM zone 10T). Locations of the 68 sites are indicated by circles with the corresponding station number. Landslide geometry is annotated on the figure with the head in the southeast and the toe in the northwest. Independent estimates of landslide thickness are available near sites 3, 15, and 22 (blue triangles). Each station is color coded by the dominant frequency of the maximum horizontal-to-vertical spectral ratio (HVSR) value. Black stations had HVSR peak frequencies above 8 Hz. Inset shows location of the Two Towers landslide in northern California (CA). The color version of this figure is available only in the electronic edition.

In June 2016, when the landslide was moving ~1 mm/week, we deployed 68 three-component 5 Hz nodal seismometers on the Two Towers landslide. The experiment geometry is shown in Figure 1 and consists of a central line of 27 seismometers trending northwest–southeast placed along the slide axis and four perpendicular lines of between 11 and 13 seismometers deployed across the central portion of the slide. The instruments were buried for deployment and recorded continuously for one week (see Data and Resources).

HVSRs and ambient noise

The HVSR is a metric commonly employed to estimate structure and seismic site effects using the ambient seismic field (Nogoshi and Igarashi, 1971; Nakamura, 1989). In addition, Sánchez-Sesma *et al.* (2011) showed that the HVSR is directly related to the Green's function (GF), allowing HVSR measurements to be used for shallow structure characterization. Under the diffuse field assumption, the spectral energies at an observed location for motion in the i direction are proportional to the autocorrelation of the observed ambient wavefield $|u_i(\mathbf{x},\omega)|^2$ (Perton *et al.*, 2009), which are proportional, after averaging, to the imaginary part of the GF $\mathrm{Im}(\mathcal{G}_{ii}(\mathbf{x},\omega)) \propto \langle |u_i(\mathbf{x},\omega)|^2 \rangle$ (Sánchez-Sesma *et al.*, 2011). Here, ω is the angular frequency, $\langle\,\rangle$ denotes the average over many time windows, and $\mathcal{G}_{ii}(\mathbf{x},\omega)$ represents the displacement in direction i resulting from a unit harmonic load applied in the same direction at location $\mathbf{x}$. Using this proportionality, the HVSR can be expressed as

$$\mathrm{HVSR}(\mathbf{x},\omega) = \sqrt{\frac{\langle |u_1(\mathbf{x},\omega)|^2\rangle + \langle |u_2(\mathbf{x},\omega)|^2\rangle}{\langle |u_3(\mathbf{x},\omega)|^2\rangle}} = \sqrt{\frac{\mathrm{Im}(\mathcal{G}_{11}(\mathbf{x},\omega) + \mathcal{G}_{22}(\mathbf{x},\omega))}{\mathrm{Im}(\mathcal{G}_{33}(\mathbf{x},\omega))}}. \quad (1)$$

In this equation, the HVSR computed from the ambient seismic field is related to local soil structure via the $\mathrm{Im}(\mathcal{G}_{ii})$ components. We compute HVSRs for the 68 stations shown in Figure 1 using equation (1).

At the frequencies important for engineering ground motions (i.e., 1–5 Hz), the origin of the ambient seismic field can be either cultural or natural (Bonnefoy-Claudet *et al.*, 2006). To explore its nature near the Two Towers earthflow, we analyze the raw seismograms to determine whether there are any systematic changes in noise character that may point to potential sources. We also explore the horizontal and vertical spectra (numerator and denominator of equation 1) individually during day and nighttime hours to isolate diurnal variations that may be indicative of an anthropogenic source. In addition, we acknowledge that the seismic wavefield at the Two Towers may not be fully diffuse. Despite this, the ambient seismic field can still be used for structure characterization (Mulargia, 2012). To enhance equipartition of the ambient wavefield, we compute the averages in equation (1) using 20 s time windows that overlap by 50% for a total time period of five days. Each time window is demeaned, detrended, and filtered between 0.2 and 40 Hz, and we apply spectral whitening to all components before evaluating equation (1) (e.g., Spica *et al.*, 2017, 2018).

Inversion for velocity structure

After computing the HVSRs, we also want to determine the physical causes of any HVSR peaks. As such, we jointly invert the HVSRs described earlier for shallow 1D velocity structure following the procedure described in detail in Perton *et al.* (2017). Several methods exist to compute the HVSR under the diffuse field assumption (e.g., García-Jerez *et al.*, 2016; Perton and Sánchez-Sesma, 2016; Perton *et al.*, 2017). Recent studies (Sánchez-Sesma *et al.*, 2011; Perton *et al.*, 2017; Spica *et al.*, 2017, 2018) have shown that the discrete wavenumber method (Bouchon, 2003) is efficient and suitable for forward modeling HVSRs for stations located at the surface or at depth.

To reduce the nonuniqueness of the problem, we invert several HVSRs along two different lines of sensors (Perton *et al.*, 2017; Spica *et al.*, 2017). The free parameters are the S-wave velocities (V_S) and the layer thicknesses for a total of two layers over a half-space. The objective function (ϵ) is defined as the root mean square (rms) difference between the observed and calculated HVSRs:

$$\epsilon = \sqrt{\frac{1}{N_x N_\omega} \sum_{x_i} \sum_{\omega} (\mathrm{HVSR}^{\mathrm{observed}} - \mathrm{HVSR}^{\mathrm{computed}})^2}. \quad (2)$$

In this expression, the observed and calculated HVSRs are normalized according to the maximum amplitude to balance the error weight between all the measurements. Here, $N_x = 11$ is the number of stations x_i used in the inversion, and $N_\omega = 30$ is the number frequencies at which spectral ratios were modeled. (These are linearly sampled between 0.8 and 14 Hz.)

Inverting the HVSR alone is not sufficient to characterize shallow structure because there is a trade-off between layer velocities and thicknesses that makes the inversion results nonunique (Piña-Flores *et al.*, 2016). Perton *et al.* (2017) showed that inverting several positions and constraining thickness and velocity variations along a profile helps retrieve coherent final structure. As such, we manually determined the combination of layer thicknesses and velocities required to produce a good fit of the HVSR at station 15 while taking into account the independent constraint on landslide thickness (7.9 m) measured by Schulz *et al.* (2018) (i.e., the top layer thickness was constrained to be close to the measured thickness, and the layer velocities were adjusted to fit the HVSR at station 15). After a good fit to the HVSR at station 15 was obtained, we then used the resulting velocity structure as a starting model for the inversion, which uses a pattern search method (Audet and Dennis, 2001) to minimize equation (2). In the inversion, we place no restrictions on the layer thickness; however, the shear-wave velocities of each layer are only allowed to vary by 15% from the value determined at station 15. Adding this constraint assumes similar structure is present along the line of sensors. This assumption is justified because the array aperture is small (i.e., 240 m), and no visible changes in lithology, porosity, or other factors would greatly influence the seismic-wave velocities.

Results

HVSR peaks and noise character

Local maxima in the HVSR are thought to represent resonances of soil-covered terrains (Haghshenas *et al.*, 2008). Two different HVSR peaks are apparent in Figure 2. First, all stations show a prominent peak between 1 and 2 Hz. We confirmed that this HVSR peak is not a result of instrument self-noise (Ringler *et al.*, 2018), and it is much lower frequency than signals attributed to persistent noise in nodes or other atmospheric phenomena (Farrell *et al.*, 2018; Johnson *et al.*, 2019). For the 68 stations, the average value of this peak is 1.23 Hz, whereas the standard deviation is 0.03 Hz, making it nearly identical across the array. This low-frequency peak is also inversely proportional to elevation; at sites near the head and to the west of the slide, this HVSR peak occurs at systematically lower frequencies than at stations to the east and near the slide toe. Second, each of the HVSR curves shown in Figure 2 also has a broad peak between 4 and 12 Hz with an average of 6.34 Hz and a standard deviation of 1.2 Hz. For each station, we determine the dominant frequency or the frequency at which the maximum HVSR occurs and color code of the station locations are shown in Figure 1 according to that frequency. Figures 1 and 2b show a clear progression from high-frequency dominant frequencies (near 8 Hz) at the toe and head to lower frequency dominant periods (near 4 Hz) in the central region of the slide. If the seismic-wave velocities within the slide do not vary considerably, the dominant frequency is thought to be inversely proportional to thickness (Haskell, 1960; Borcherdt, 1970; Yamanaka *et al.*, 1994); hence, these variations likely reflect slide geometry with lower frequency HVSR peaks corresponding to thicker deposits and vice versa. To explore this possibility, we invert the HVSRs for shallow velocity structure. The cross-slide dominant frequencies are more variable. Abrupt changes in elevation, variable thickness of unconsolidated surface material, and 2D structure may be the main controls on the dominant frequency at these sites.

Analysis of daily seismograms indicates that there is a strong noise source of anthropogenic origin in the data. This source manifests as a high-amplitude signal that begins at approximately 11:30 local time and terminates around 5 p.m. (see Fig. S1, available in the supplemental material to this article). To further investigate the effect of this source, we examined the HVSRs at night and during the day for all stations (see Fig. S2). Although both high- and low-frequency HVSR peaks are apparent at all stations during nighttime hours (i.e., between 7 p.m. and 7 a.m. local time), during daytime hours, the peaks are greatly diminished in amplitude for all stations in the deployment (e.g., Fig. S3). In some cases, the low-frequency HVSR peak disappears entirely. This variation is primarily due to local minima in the vertical-component spectra that are much smaller during nighttime hours than during the day. This gives rise to more prominent (i.e., higher amplitude) HVSR peak during nighttime hours.

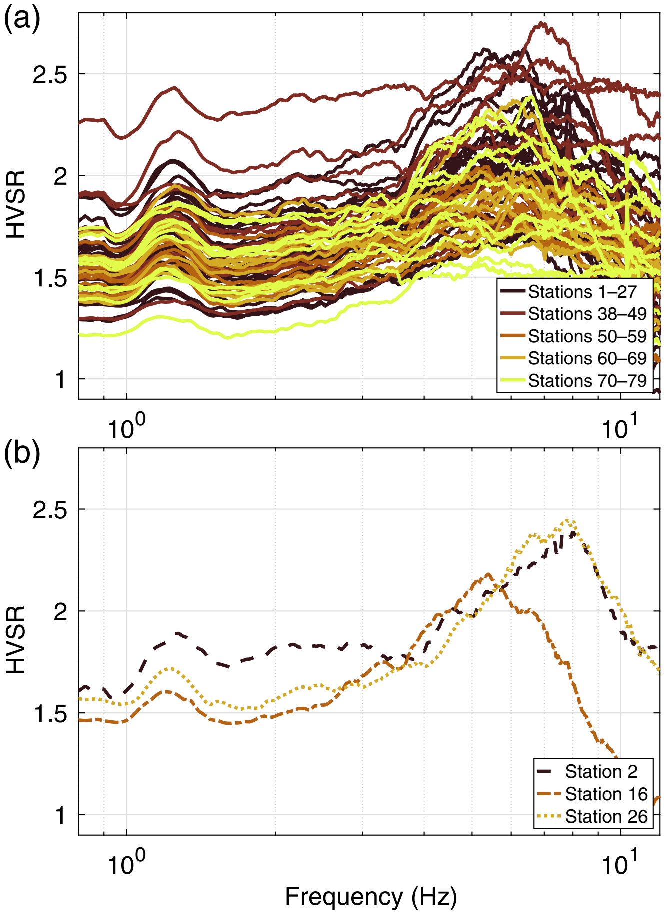

Figure 2. (a) Computed HVSRs for the 68 stations in the deployment. Two different resonances (i.e., local maxima in the HVSR) are present at all stations. The lower frequency resonance averages 1.23 Hz across all stations, whereas the higher frequency resonance occurs above 4 Hz at all stations. (b) HVSRs for stations 2, 16, and 26 at the slide toe, middle, and head, respectively. There is a clear shift in dominant frequency from near 8 Hz at stations 2 and 26 to near 5 Hz at station 16. The color version of this figure is available only in the electronic edition.

Landslide structure

We invert the HVSR for the velocity structure along two orthogonal lines using the technique described in the Methods section. The first line is oriented downslope and includes stations 3–23, all of which locate along the slide axis. Fits to the HVSRs at the stations and the results of the inversion are shown in

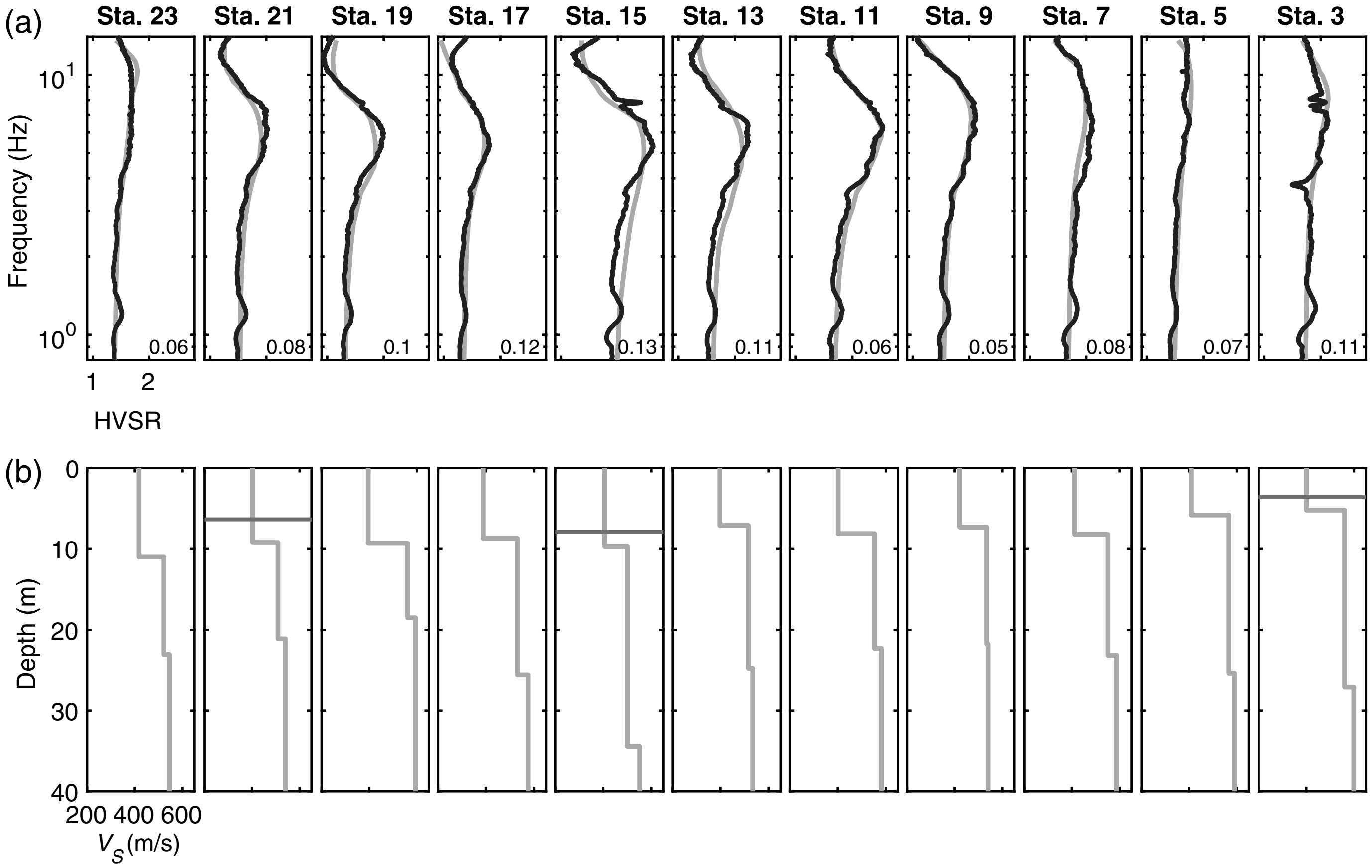

Figure 3. (a) Measured HVSRs (black) and fits (gray) for stations (Sta.) 3–23 used in the inversion for structure along the slide axis. The root mean square (rms) difference between the modeled and observed HVSRs is shown in the bottom right of each station plot. (b) Best-fitting 1D shear-wave velocity models below each station. Horizontal gray lines indicate field measurements of the approximate depth to the shear zone.

Figure 3a,b, respectively. Because we are interested in very shallow structure, we did not attempt to fit the low-frequency HVSR peak in our inversion. Rms misfits are shown in the bottom right of Figure 3a. The 1D velocity structure at all stations is highly similar and is characterized by a relatively low-velocity shallow layer overlying a higher velocity substrate. The top (i.e., shallowest) layer in the model is an average of 8.15 m thick and has relatively homogeneous velocity averaging $V_S =$ 405 m/s with variance <4.1% at the 11 different stations. In addition, the velocity of the top layer at each station deviates by no more than 8.4% from the value at station 15, far less than the 15% allowed in the inversion. The thickness of the top layer in the model varies between 5.2 m at station 3, close to the slide toe, and 11 m at station 23. In all cases, the thickness of the top layer exceeds the measured thicknesses (Schulz *et al.*, 2018) indicated by horizontal gray lines in Figure 3. The largest velocity contrast in the model occurs between the top and middle layers, with the middle layer averaging 537 m/s, an increase of >30% in velocity from the shallowest layer. The middle layer is also more than three times thicker than the top layer on average. In all 1D profiles, a much smaller velocity increase exists at depths of >18.5 m. In all profiles, the velocity increase between the middle and bottom layers does not exceed 10.3%. We note that the HVSR technique loses resolution with depth, and these deeper velocity contrasts may be due to gradual increases in velocity with depth rather than abrupt contrasts. Because there is a noise source of anthropogenic origin in the data, we also inverted only the nighttime HVSRs for subsurface structure. The results previously discussed do not change significantly.

In addition to the line along the slide axis, we also inverted the HVSRs for a line of stations deployed perpendicular to the slide axis. We discuss this cross-slide profile in detail in the supplemental material; however, the presence of structural heterogeneity such as lateral shear margins, gullies, sharp topographic gradients, and so forth, across the slide body violates the assumption that the HVSR results from the 1D velocity structure below each station. Therefore, we do not consider this profile in our interpretation of landslide geometry.

Discussion

HVSR peaks, such as those present at 1.23 Hz and above 4 Hz in Figure 2, can be caused by a number of different factors

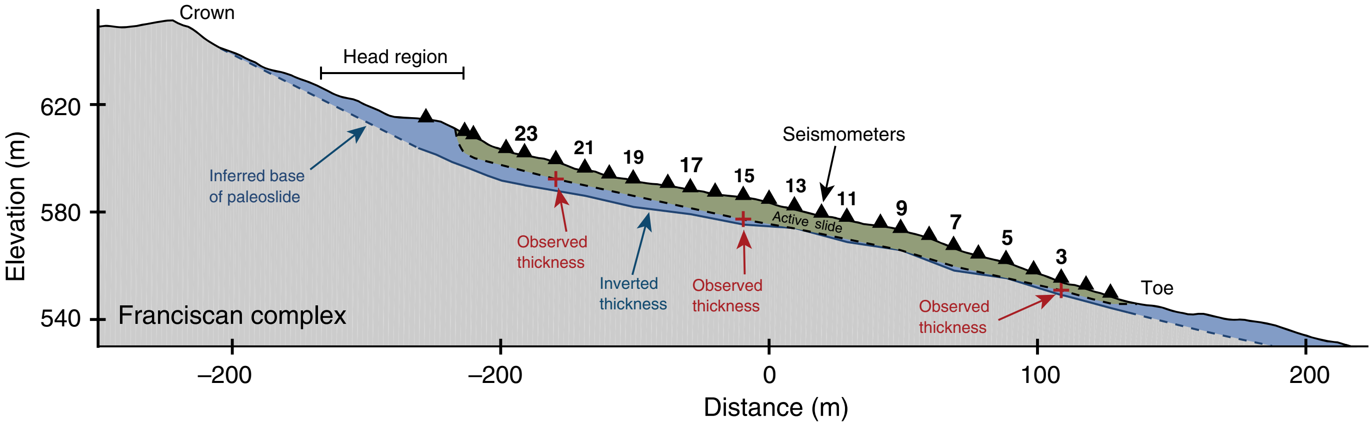

Figure 4. Schematic cross section of the Two Towers earthflow. The color version of this figure is available only in the electronic edition.

depending on their frequency. HVSR peaks near 1 Hz were observed in spectral ratios derived from both the ambient seismic field and local earthquakes recorded at landslides in the eastern San Francisco Bay region and were interpreted as topographic resonances (Hartzell *et al.*, 2014, 2017). The resonance frequency of a topographic feature can be estimated using $f = V_S/L$, in which L is the width of the feature (Bouchon, 1973). Using estimates for seismic-wave velocity for metagraywacke (the dominant rock type within the Franciscan Complex) from Brocher (2008) and a V_P/V_S ratio from Pasyanos *et al.* (1996), we find a shallow V_S of 921 m/s for a depth of 1 km corresponding to a $L = 750$ m. A cursory survey of topographic features nearby the Two Towers slide does not reveal topographic prominences of that dimension. A second possibility is that the 1.23 Hz resonance is the result of either standing waves within the slide deposit itself or the resonance of compliant fractures within the slide body (Moore *et al.*, 2011). Because the 1.23 Hz resonance is observed at stations both on and off the slide, we rule out these mechanisms. A third possibility is that deeper velocity structure gives rise to the 1.23 Hz peak in the HVSR. Spica *et al.* (2018) were able to fit a low-frequency resonance at 0.4 Hz with a velocity model that contained a strong velocity contrast at 800 m depth; hence, fitting the 1.23 Hz peak would require a significant velocity contrast at a few hundred meters of depth. Given the highly variable nature of Franciscan Complex, such a velocity contrast is a possibility, and this is our preferred interpretation of this peak.

The higher frequency resonances (i.e., those >4 Hz) systematically vary from near 8 Hz at the slide head and toe to near 4 Hz in the center, suggesting that the high-frequency part of the measured HVSR reflects the thickness of shallow slide deposits. After inverting the HVSRs in the along-slide profile for shallow structure, we find that the shallowest layer in the model has a velocity near 400 m/s and thicknesses between 5.2 and 11 m. Because of the relatively large velocity contrast between the shallow and middle layers of the velocity structure, we interpret the shallow layer in the along-slide inversion to reflect the depth extent of landslide-related deposits. The relatively low velocity of the shallowest layer likely results from extension-related dilation of slide materials, whereas the impedance contrast between the top and middle layers suggests that the slide sits atop more consolidated material. Previous landslide imaging studies have noted that the application of smoothing constraints in tomographic inversions obscures the location of the landslide boundaries (Renalier *et al.*, 2010; Pilz *et al.*, 2014); the HVSR technique we apply here does not suffer from this limitation.

The HVSR inversion produces thicknesses that are systematically larger than those measured *in situ*. One possible explanation for this discrepancy is that the depths and slip surfaces determined from slope inclinometer profiles are not the deepest extent of the unstable slide body. Figure 4 shows a schematic cross section of the slide that relates the inverted thicknesses we determine here to the field observations of Schulz *et al.* (2018). The Two Towers earthflow is a reactivation (age unknown) of a landslide deposit more than twice its length. Nested slides contain actively sliding material that is thinner and smaller in scale than the larger slide deposit and are common in earthflow complexes such as the region surrounding the active Two Towers earthflow (e.g., Williams and Pratt, 1996). The velocity contrasts imaged with the HVSR technique may reflect the depth of the larger slide deposit in most areas. This interpretation, shown in Figure 4, is further supported by the observation of a shallow low-velocity layer at the stations that were deployed off the active slide body, which likely reflects shallow colluvium beyond the lateral margins of the active slide (Fig. S4). In addition, earthflows in the region commonly occur within landslide deposits and colluvium of similar composition that extend to greater depth, with no apparent contrast in materials from within to below the active slides (Keefer and Johnson, 1983; Iverson and Major, 1987).

Geophysical analyses of landslides are often motivated by assessing landslide hazard. Because the high-frequency HVSR peaks measured at Two Towers are caused by shallow slide deposits and represent frequencies that will experience amplification during earthquakes, the depth of the actively sliding mass measured by Schulz *et al.* (2018) may be less relevant for assessing potential slide volume and associated hazard than the thicknesses determined by our inversions. If our interpretation that the thickness of this layer corresponds to the depth extent of an older, larger slide body, this suggests that the local geomorphic history can be an important factor in determining landslide site response. More generally, our results underscore the utility of combining both geotechnical measurements and subsurface imaging for landslide characterization and hazard assessment.

Summary and Conclusions

We deployed a network of 68 nodes on a slow-moving earthflow in northern California to study site response and structure on the scale of an individual landslide. We showed that there are two prominent peaks in the noise-derived HVSRs at all stations deployed both on and off the Two Towers earthflow. The first peak is close to 1.23 Hz at all stations and could be due to a several-hundred-meter-deep velocity contrast, although the exact origin is unknown. The higher frequency peak in the HVSR occurs between 4 and 8 Hz on most stations and is interpreted to result from shallow slide deposits. Using *a priori* constraints from *in situ* thickness measurements, we invert the HVSR for local velocity structure. A shallow low-velocity layer averaging 8 m thick likely reflects the extent of paleoslide deposits because the inverted low-velocity layer thicknesses are systematically larger than those measured *in situ*. More generally, combining geotechnical measurements, dense sensor networks, and geophysical inversion can lead to useful insights into landslide character and site response, both of which are valuable for assessing earthquake-induced landslide hazard.

Data and Resources

Figure 1 was created using the Generic Mapping Tools (GMT) software (Wessel *et al.*, 2013). Data from the University of Oregon nodal deployment on the Two Towers earthflow are available by contacting the corresponding author. The supplemental material includes additional analysis and figures that support the conclusions of the main text.

Acknowledgments

The authors thank Gillean Arnoux, Quentin Bletery, Paul Richardson, Nathan Schachtman, Sam Shaw, and Brandon VanderBeek for fieldwork assistance. The authors thank Mathieu Perton for his help in developing the horizontal-to-vertical spectral ratio (HVSR) codes. J. J. R. and W. H. S. were supported by National Aeronautics and Space Administration (NASA) Award Number NNX15AR59G. A. M. T. was supported by National Science Foundation (NSF) Award Number 1848302. The authors thank Joan Gomberg and Fan-chi Lin for carefully reviewing various versions of the article.

References

Audet, C., and J. E. Dennis Jr. (2001). Pattern search algorithms for mixed variable programming, *SIAM J. Optim.* **11,** no. 3, 573–594.

Bird, J. F., and J. J. Bommer (2004). Earthquake losses due to ground failure, *Eng. Geol.* **75,** no. 2, 147–179.

Bonnefoy-Claudet, S., F. Cotton, and P.-Y. Bard (2006). The nature of noise wavefield and its applications for site effects studies: A literature review, *Earth Sci. Rev.* **79,** nos. 3/4, 205–227.

Bonnefoy-Claudet, S., A. Köhler, C. Cornou, M. Wathelet, and P.-Y. Bard (2008). Effects of Love waves on microtremor H/V ratio, *Bull. Seismol. Soc. Am.* **98,** no. 1, 288–300.

Borcherdt, R. D. (1970). Effects of local geology on ground motion near San Francisco Bay, *Bull. Seismol. Soc. Am.* **60,** no. 1, 29–61.

Bouchon, M. (1973). Effect of topography on surface motion, *Bull. Seismol. Soc. Am.* **63,** no. 2, 615–632.

Bouchon, M. (2003). A review of the discrete wavenumber method, *Pure Appl. Geophys.* **160,** nos. 3/4, 445–465.

Brocher, T. M. (2008). Compressional and shear-wave velocity versus depth relations for common rock types in northern California, *Bull. Seismol. Soc. Am.* **98,** no. 2, 950–968.

Delbridge, B. G., R. Bürgmann, E. Fielding, S. Hensley, and W. H. Schulz (2016). Three-dimensional surface deformation derived from airborne interferometric UAVSAR: Application to the Slumgullion landslide, *J. Geophys. Res.* **121,** no. 5, 3951–3977.

Farrell, J., S.-M. Wu, K. M. Ward, and F.-C. Lin (2018). Persistent noise signal in the Fairfield Nodal three-component 5-Hz geophones, *Seismol. Res. Lett.* **89,** no. 5, 1609–1617.

García-Jerez, A., J. Piña-Flores, F. J. Sánchez-Sesma, F. Luzón, and M. Perton (2016). A computer code for forward calculation and inversion of the H/V spectral ratio under the diffuse field assumption, *Comput. Geosci.* **97,** 67–78.

Haghshenas, E., P.-Y. Bard, N. Theodulidis, and SESAME WP04 Team (2008). Empirical evaluation of microtremor H/V spectral ratio, *Bull. Earthq. Eng.* **6,** no. 1, 75–108.

Handwerger, A. L., J. J. Roering, D. A. Schmidt, and A. W. Rempel (2015). Kinematics of earthflows in the northern California Coast Ranges using satellite interferometry, *Geomorphology* **246,** 321–333.

Hartzell, S., A. L. Leeds, and R. W. Jibson (2017). Seismic response of soft deposits due to landslide: The Mission Peak, California, landslide, *Bull. Seismol. Soc. Am.* **107,** no. 5, 2008–2020.

Hartzell, S., M. Meremonte, L. Ramírez-Guzmán, and D. McNamara (2014). Ground motion in the presence of complex topography: Earthquake and ambient noise sources, *Bull. Seismol. Soc. Am.* **104,** no. 1, 451–466.

Haskell, N. A. (1960). Crustal reflection of plane SH waves, *J. Geophys. Res.* **65,** no. 12, 4147–4150.

Hovius, N., P. Meunier, C.-W. Lin, H. Chen, Y.-G. Chen, S. Dadson, M.-J. Horng, and M. Lines (2011). Prolonged seismically induced erosion and the mass balance of a large earthquake, *Earth Planet. Sci. Lett.* **304,** nos. 3/4, 347–355.

Huang, R., and X. Fan (2013). The landslide story, *Nature Geosci.* **6,** no. 5, 325–326.

Hungr, O., S. Leroueil, and L. Picarelli (2014). The Varnes classification of landslide types, an update, *Landslides* **11,** no. 2, 167–194.

Iverson, R. M., and J. J. Major (1987). Rainfall, ground-water flow, and seasonal movement at Minor Creek landslide, northwestern

California: Physical interpretation of empirical relations, *Geol. Soc. Am. Bull.* **99,** no. 4, 579–594.

Johnson, C. W., F. Vernon, N. Nakata, and Y. Ben-Zion (2019). Atmospheric processes modulating noise in Fairfield Nodal 5 Hz geophones, *Seismol. Res. Lett.* doi: 10.1785/0220180383.

Jongmans, D., and S. Garambois (2007). Geophysical investigation of landslides: A review, *Bull. Soc. Géol. France* **178,** no. 2, 101–112.

Keefer, D. K., and A. M. Johnson (1983). Earth flows: Morphology, mobilization, and movement, *Tech. Rep. U.S. Geol. Surv. Profess. Pap. 1264*, doi: 10.3133/pp1264.

Lin, G.-W., H. Chen, Y.-H. Chen, and M.-J. Horng (2008). Influence of typhoons and earthquakes on rainfall-induced landslides and suspended sediments discharge, *Eng. Geol.* **97,** nos. 1/2, 32–41.

Méric, O., S. Garambois, J.-P. Malet, H. Cadet, P. Gueguen, and D. Jongmans (2007). Seismic noise-based methods for soft-rock landslide characterization, *Bull. Soc. Géol. France* **178,** no. 2, 137–148.

Moore, J. R., V. Gischig, J. Burjanek, S. Loew, and D. Fäh (2011). Site effects in unstable rock slopes: Dynamic behavior of the Randa instability (Switzerland), *Bull. Seismol. Soc. Am.* **101,** no. 6, 3110–3116.

Mulargia, F. (2012). The seismic noise wavefield is not diffuse, *J. Acoust. Soc. Am.* **131,** no. 4, 2853–2858.

Nakamura, Y. (1989). A method for dynamic characteristics estimation of subsurface using microtremor on the ground surface, *Q. Rep. Railway Tech. Res. Inst.* **30,** no. 1, 25–33.

Nogoshi, M., and T. Igarashi (1971). On the amplitude characteristics of microtremor (part 2), *Zisin* **24,** no. 1, 26–40.

Owen, L. A., U. Kamp, G. A. Khattak, E. L. Harp, D. K. Keefer, and M. A. Bauer (2008). Landslides triggered by the 8 October 2005 Kashmir earthquake, *Geomorphology* **94,** nos. 1/2, 1–9.

Pasyanos, M. E., D. S. Dreger, and B. Romanowicz (1996). Toward real-time estimation of regional moment tensors, *Bull. Seismol. Soc. Am.* **86,** no. 5, 1255–1269.

Pazzi, V., S. Morelli, and R. Fanti (2019). A review of the advantages and limitations of geophysical investigations in landslide studies, *Int. J. Geophys.* **2019,** doi: 10.1155/2019/2983087.

Pazzi, V., L. Tanteri, G. Bicocchi, M. D'Ambrosio, A. Caselli, and R. Fanti (2017). H/V measurements as an effective tool for the reliable detection of landslide slip surfaces: Case studies of Castagnola (La Spezia, Italy) and Roccalbegna (Grosseto, Italy), *Phys. Chem. Earth* **98,** 136–153.

Perton, M., and F. J. Sánchez-Sesma (2016). Green's function calculation from equipartition theorem, *J. Acoust. Soc. Am.* **140,** no. 2, 1309–1318.

Perton, M., F. J. Sánchez-Sesma, A. Rodríguez-Castellanos, M. Campillo, and R. Weaver (2009). Two perspectives on equipartition in diffuse elastic fields in three dimensions, *J. Acoust. Soc. Am.* **126,** no. 3, 1125–1130.

Perton, M., Z. Spica, and C. Caudron (2017). Inversion of the horizontal-to-vertical spectral ratio in presence of strong lateral heterogeneity, *Geophys. J. Int.* **212,** no. 2, 930–941.

Pilz, M., S. Parolai, D. Bindi, A. Saponaro, and U. Abdybachaev (2014). Combining seismic noise techniques for landslide characterization, *Pure Appl. Geophys.* **171,** no. 8, 1729–1745.

Piña-Flores, J., M. Perton, A. García-Jerez, E. Carmona, F. Luzón, J. C. Molina-Villegas, and F. J. Sánchez-Sesma (2016). The inversion of spectral ratio H/V in a layered system using the diffuse field assumption (DFA), *Geophys. J. Int.* **208,** 577–588.

Renalier, F., D. Jongmans, M. Campillo, and P.-Y. Bard (2010). Shear wave velocity imaging of the Avignonet landslide (France) using ambient noise cross correlation, *J. Geophys. Res.* **115,** no. F3, doi: 10.1029/2009JF001538.

Ringler, A., R. E. Anthony, M. Karplus, A. Holland, and D. Wilson (2018). Laboratory tests of three Z-land Fairfield Nodal 5-Hz, three-component sensors, *Seismol. Res. Lett.* **89,** no. 5, 1601–1608.

Sánchez-Sesma, F. J., M. Rodríguez, U. Iturrarán-Viveros, F. Luzón, M. Campillo, L. Margerin, A. García-Jerez, M. Suarez, M. A. Santoyo, and A. Rodriguez-Castellanos (2011). A theory for microtremor H/V spectral ratio: Application for a layered medium, *Geophys. J. Int.* **186,** no. 1, 221–225.

Schulz, W. H., J. B. Smith, G. Wang, Y. Jiang, and J. J. Roering (2018). Clayey landslide initiation and acceleration strongly modulated by soil swelling, *Geophys. Res. Lett.* **45,** 1888–1896, doi: 10.1002/2017GL076807.

Spica, Z., M. Perton, N. Nakata, X. Liu, and G. C. Beroza (2018). Shallow Vs imaging of the Groningen area from joint inversion of multi-mode surface waves and H/V spectral ratios, *Seismol. Res. Lett.* **89,** 1720–1729, doi: 10.1785/0220180060.

Spica, Z. J., M. Perton, N. Nakata, X. Liu, and G. C. Beroza (2017). Site characterization at Groningen gas field area through joint surface-borehole H/V analysis, *Geophys. J. Int.* **212,** no. 1, 412–421, doi: 10.1093/gji/ggx426.

Wessel, P., W. H. Smith, R. Scharroo, J. Luis, and F. Wobbe (2013). Generic mapping tools: Improved version released, *Eos Trans. AGU* **94,** no. 45, 409–410.

Williams, R. A., and T. L. Pratt (1996). Detection of the base of Slumgullion landslide, Colorado, by seismic reflection, in *The Slumgullion Earth Flow: A Large-Scale Natural Laboratory*, D. J. Varnes and W. Z. Savage (Editors), U.S. Geological Survey Bulletin, Denver, Colorado77–83.

Yamanaka, H., M. Takemura, H. Ishida, and M. Niwa (1994). Characteristics of long-period microtremors and their applicability in exploration of deep sedimentary layers, *Bull. Seismol. Soc. Am.* **84,** no. 6, 1831–1841.

Yin, Y., F. Wang, and P. Sun (2009). Landslide hazards triggered by the 2008 Wenchuan earthquake, Sichuan, China, *Landslides* **6,** no. 2, 139–152.

Manuscript received 1 August 2019